Report on the first two years of seismic characterisation of the Sos Enattos former mine

ET-0359A-21

L. Naticchioni[1], G. Saccorotti[2], et al. [ET Sardegna Seismic Characterisation group*]

1. *INFN Roma*
2. *INGV Pisa*

Abstract. In this document we summarize the results achieved in the first two years of seismic characterisation of the Sos Enattos former mine, the candidate site for ET in Sardinia, Italy. A bibliography with the related and already published works is provided at the end of this note.

25 June 2021

*ET Sardegna Seismic Characterisation Group:
A. Allocca, T. Andric, D. Barrale, A. Berbellini, L. Boschi, E. Calloni, L. Cardello, A. Cardini, M. Carpinelli, A. Contu, R. De Rosa, A. Dell'Aquila, F. Dettori, L. Di Fiore, M. Di Giovanni, F. Dordei, D. D'Urso, L. Errico, V. Fanti, I. Fiori, C. Giunchi, A. Grado, J. Harms, S. Koley, E. Majorana, M. Marsella C. Migoni, L. Naticchioni, G. Oggiano, M. Olivieri, F. Paoletti, M. Punturo, P. Puppo, P. Rapagnani, F. Ricci, R. Romero, D. Rozza, G. Saccorotti, V. Sipala, I. Tosta, M.C. Tringali, L. Trozzo

Table of Contents.

1. Introduction.

In March 2019 we started an extensive seismic monitoring of the Sos Enattos site in the framework of the site characterisation for the Einstein Telescope (ET). The sensor network installed in Sos Enattos is composed of one surface seismic station (SOE0), three underground stations at different depth (SOE1 at -84m, SOE2 at -111m and SOE3 at -160m) and a control room in the SarGrav surface laboratory. They are all equipped with broadband triaxial seismometers as reported in **Table 1**. Moreover, in January 2021 we deployed on the hill above the underground tunnel of the mine a temporary seismometers array composed of 15 seismometers provided by INGV and INFN.

Station code	Depth WRT surface	Sensor installed	Period	Digitiser
SOE0 (2019)	0 (338 a.s.l.)	Guralp 3EPSCD 120	2019/3-2019/12	Embedded
SOE0 (2020)	0 (400m asl)	Nanometrics Trillium 240	2019/12-...	Nanometrics Taurus
SOE1 (2019)	-84m (254m asl)	Nanometrics Trillium 240	2019/3-2020/7	Nanometrics Taurus
SOE1 (2020)	-84m (254m asl)	Nanometrics Trillium 120H	2020/7-...	Nanometrics Centaur
SOE2	-111m (227m asl)	Nanometrics Trillium 240	2019/3-...	Nanometrics Taurus
SOE3	-160m (178m asl)	Nanometrics Trillium 240	2020/8-...	Nanometrics Taurus

***Table 1**: stations of the Sos Enattos seismic network [3].*

2. Sensor deployment.

The surface station (SOE0) was initially located in a prefabricated hut close to the SarGrav control room, equipped with a Guralp 3ESPCD seismometer. This installation proved to be not optimal, therefore we decided to move the location about 210m away from the control room, with a vault installation. Also the sensor was replaced with a more reliable Nanometrics Trillium 240 (from now on T240) installed in December 2019. This upgrade ensured an improvement of the measured data, in particular from the horizontal signal and below 0.1Hz.
The first underground station (SOE1) is located in a small cave along the former mine tunnel (called "rampa Tupeddu", **Fig.1**), at about 84m below the surface (vertical depth). Two big granite blocks cemented to the bedrock ensures a good mechanical coupling with the ground. Here we installed initially (March 2019) another T240, eventually replaced (2020/7) by a Nanometrics Trillium 120 Horizon (from now on T120H). In particular, with the new sensor installation we decided to adopt a reduced input range (4Vpp with respect to the

standard 40Vpp) in the digitiser, a Nanometrics Centaur. With these settings we demonstrated, as reported in the following sections, that in the few-Hz band the initial measures were limited by the acquisitor self-noise when operated with standard input range, given the peculiar low background noise at the site.

The second station (SOE2) is located in a cave along the tunnel, at -111m with respect to the surface (vertical depth). Here, from March 2019 we installed a T240 on the top of a granite block cemented to the bedrock. The seismometer at this station is integrated in the national seismological network of the INGV, for this reason its digitiser operates with the standard input range settings.

The third and last underground station is located at the end of the "rampa Tupeddu", along the side of the tunnel, at about -160m from the surface (vertical depth). Here, in August 2020, we installed a T240, placed on a granite tile cemented to the bedrock.
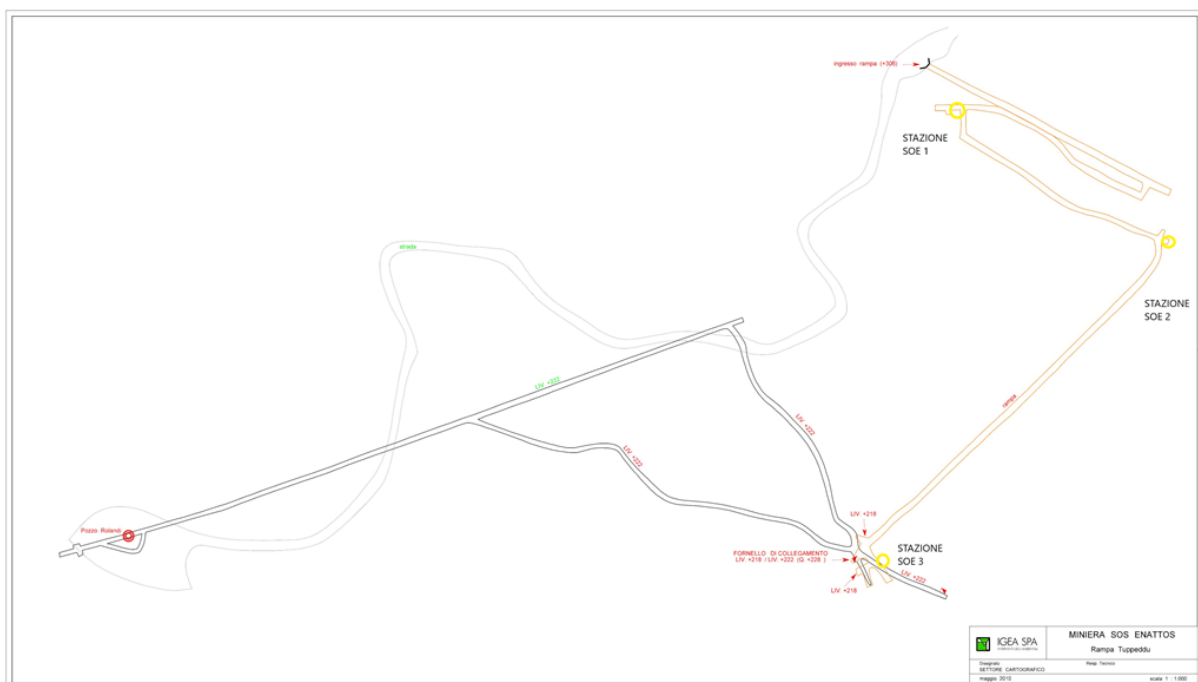

Fig.1. *location of the underground seismic stations at the Sos Enattos former mine along the underground tunnel "Rampa Tupeddu".*

The data produced by the surface station SOE0 is transmitted to an INGV server through a UMTS mobile link. All the other underground stations are connected to the SarGrav control room through a local network with an optical fiber link. A GPS timing reference signal is distributed to the stations through the network for data synchronisation. The data acquired at the control room is then transmitted to an INGV server through another UMTS mobile link.

Finally, the data acquired in the INGV server is copied and stored in the official ET Repository, where it can be accessed for analysis.

3. Seismic background noise.

In **Fig.2** we show the probabilistic power spectral densities (PPSD) of the vertical acceleration [3] for the surface station SOE0 and the underground station SOE2 in the first

quadrimester of 2020. The shapes are very similar up to 10Hz, but in both cases this measure is limited by the self noise of the DAQs, which are operated with the standard input range settings. The general features of these spectra follow Peterson's NLNM, with the prominent peaks produced by the microseisms between 0.1 Hz and 1 Hz. The minimum is at 3.5 Hz (-154 dB) in SOE0 and 4.5Hz (-157dB) at SOE2. Both the PPSD meet the ET noise requirements of -154 dB at 4 Hz. The day-night pattern can be observed only above 2 Hz, with a maximum difference of about 5 dB (a factor 1.8 in amplitude) [3].
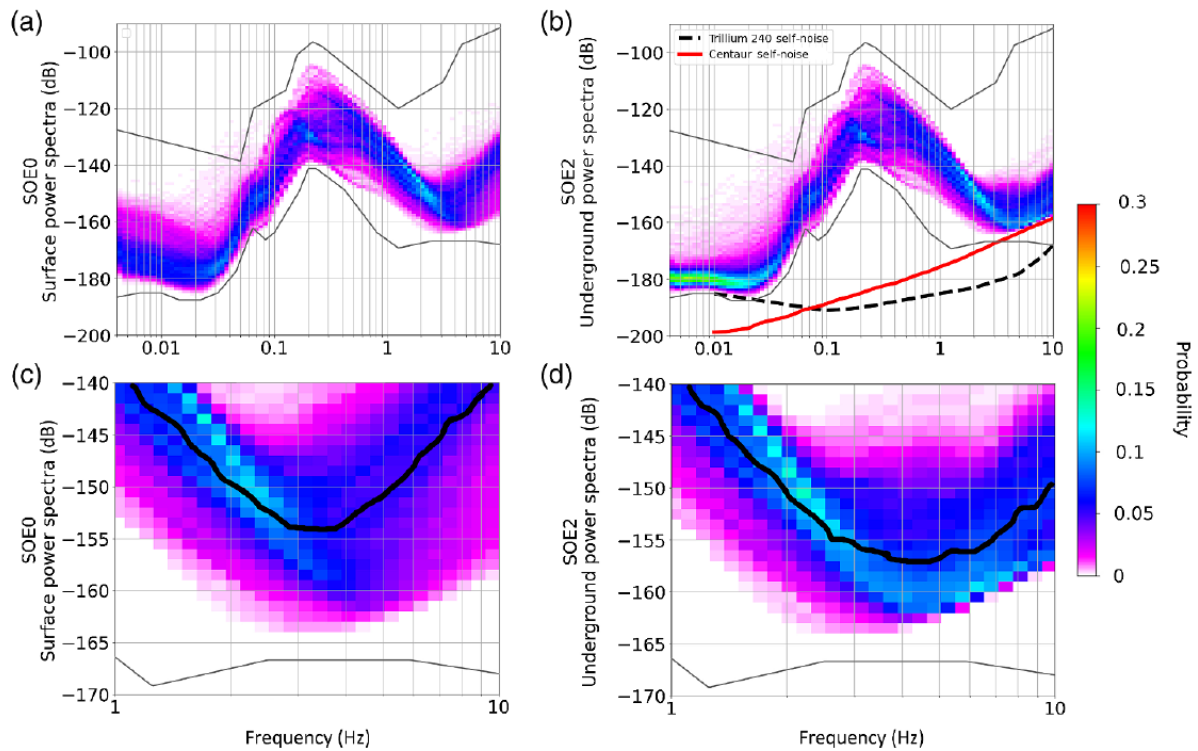

Fig.2. probabilistic power spectral densities (PPSD) of the vertical channels from surface (SOE0 station) and -111m underground (SOE2 station) during the 2020 [3]. For comparison also the Peterson's model curves (NLNM, new low noise model, and NHNM, new high noise model) are drawn. Note that both stations are operated without amplification, with the standard input range of 40Vpp at the digitizers.

In **Fig. 3** we report the vertical and horizontal PPSD in the first half of 2021 from three stations: SOE0, SOE1, SOE2. In this case SOE1 is operated with a reduced input range, guaranteeing a lower DAQ self-noise. Comparing the PPSD of SOE1 to the other two stations, it is clear that the noise floor in Sos Enattos between 2 Hz and 7 Hz reaches the minimum defined by the NLNM. This is evident also by comparing the data from the same station SOE1 before and after the change of the input range (**Fig. 4**).

In **Fig. 5** we plot the median and floor from SOE1 (reduced input range) and SOE2 (standard settings) for the period June to October 2020. From this plot we note that the medians are very similar, while the noise floors follow the Person's NLNM.

In the band 4 Hz - 7Hz, the rating of the SOE2 station at Sos Enattos in the global seismic network (where it is named SENA) is among the 10% quietest sites in the world (**Fig.6**, [3]), and the rating is even better if we consider the data acquired with SOE1 with the reduced input range of the digitiser.
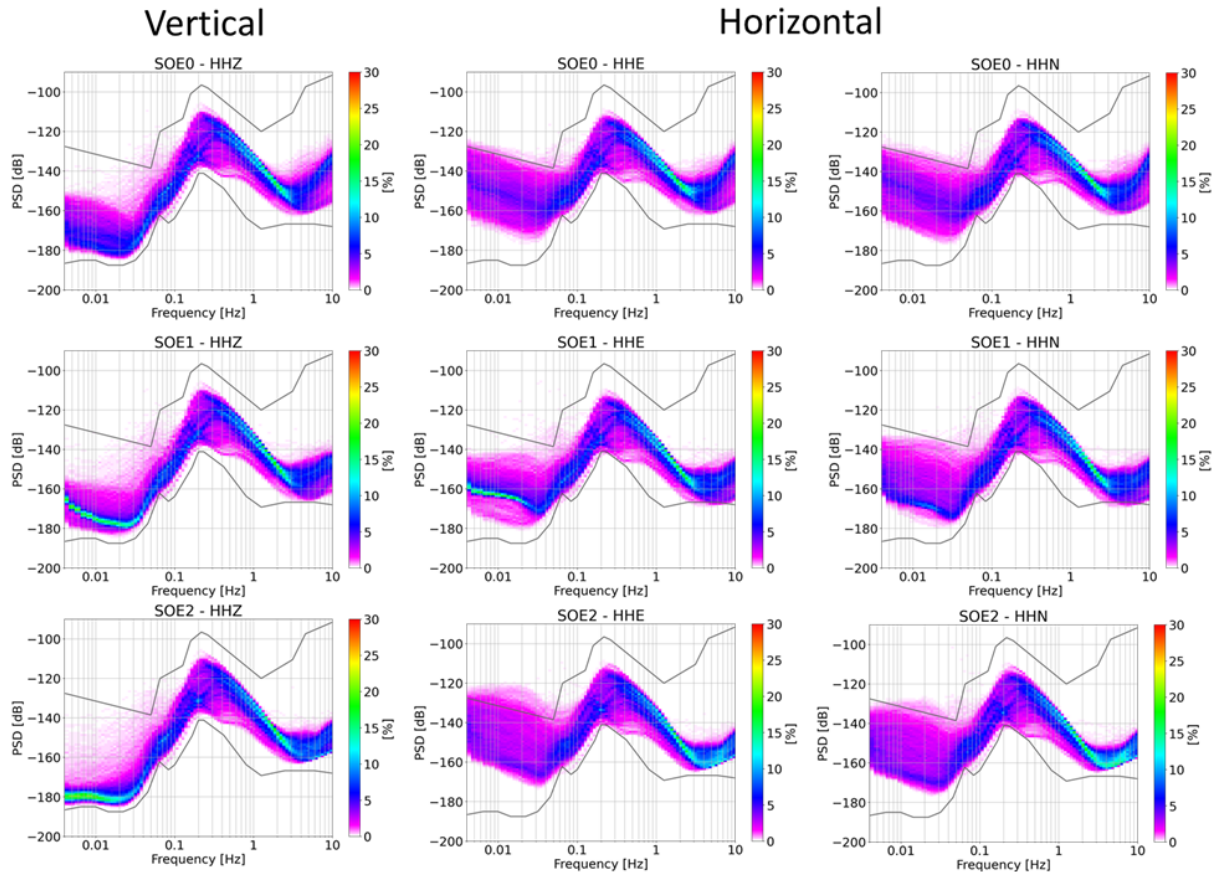
Fig.3. *probabilistic power spectral densities (PPSD) of the vertical and horizontal channels from surface (SOE0) and underground stations (SOE1, -84m, and SOE2, -111m) during the first half of 2021. For comparison also the Peterson's model curves (NLNM, new low noise model, and NHNM, new high noise model) are drawn. SOE0 and SOE2 are operated without amplification, with the standard input range of 40Vpp at the digitizers, while SOE1 is operated with the reduced input range of 4Vpp: in this case the improvement in the measure can be observed from 3Hz to 10Hz, indeed in this band the digitiser self-noise sets a limit to the measured noise in the other stations operated with standard settings.*
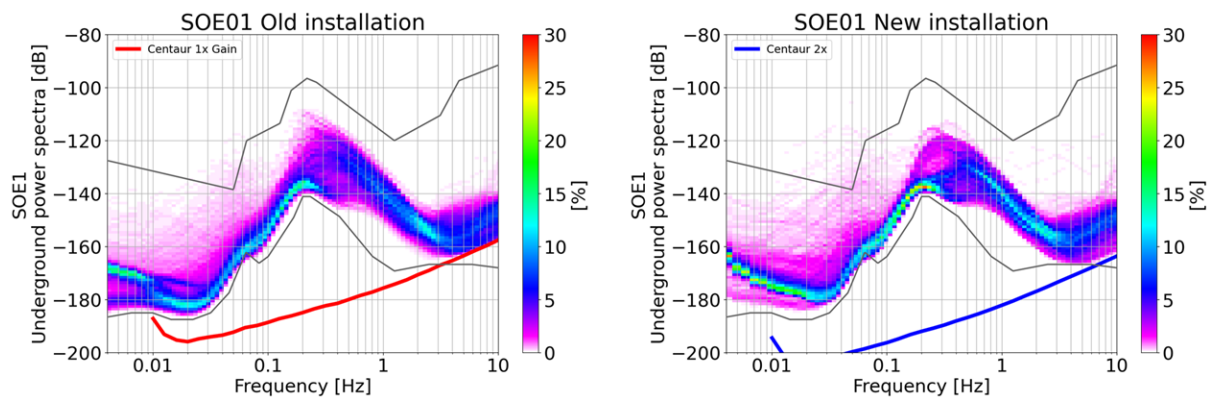

Fig.4. *the vertical PPSD measured in station SOE1 before and after the change of the ampification (i.e. of the input range). The red and blue lines indicate respectively the self-noise for the input ranges 40Vpp and 4Vpp.*
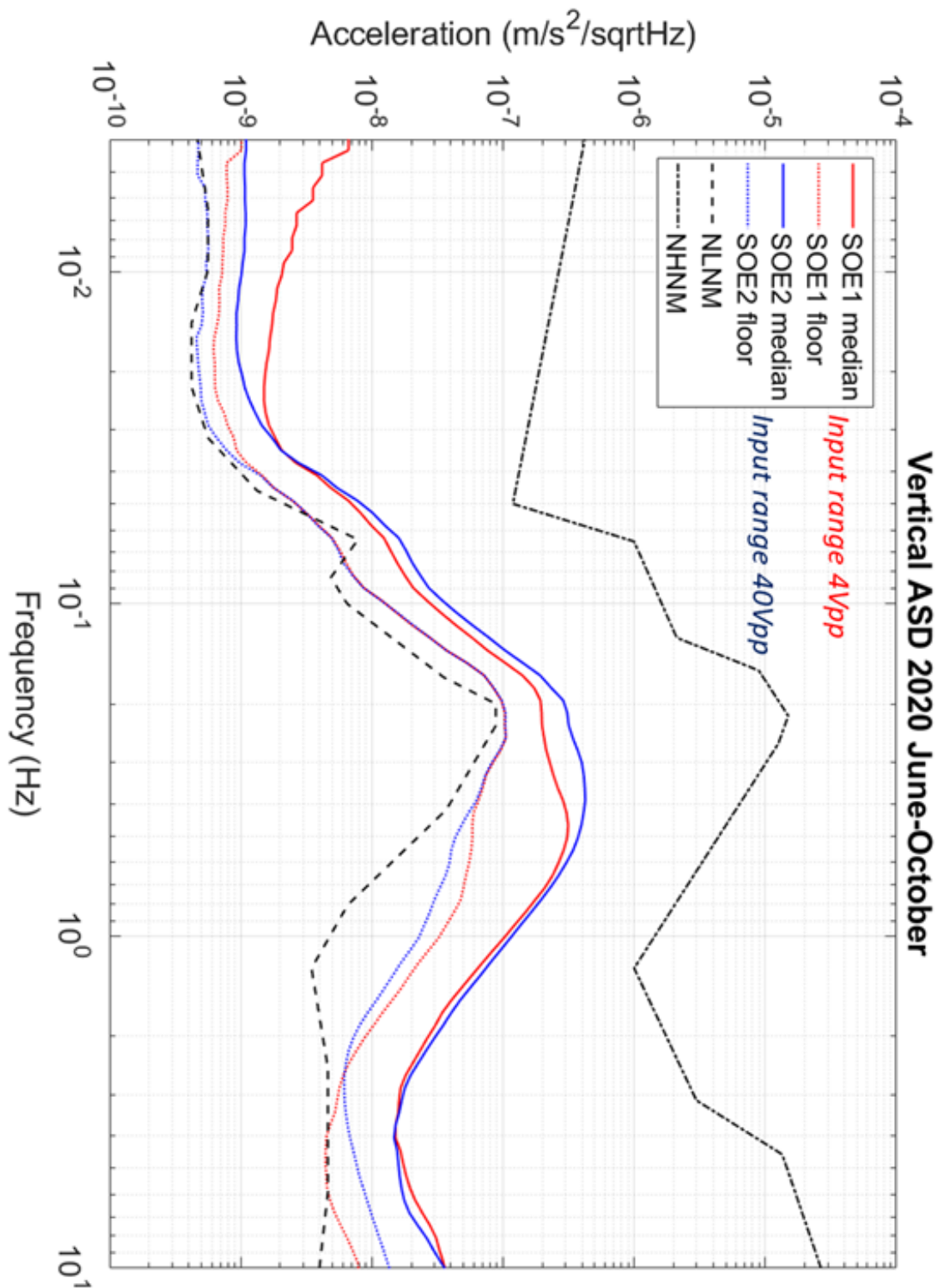
Fig.5. *Comparison of the median and floor seismic noise level in SOE1 (reduced input range, in red) and SOE2 (standard settings, in blue), compared with the NLNM and NHNM, for the period June to October 2020. The reduced input range at SOE1 allows the observation of the seismic noise floor around 4 Hz, which follows the NLNM.*
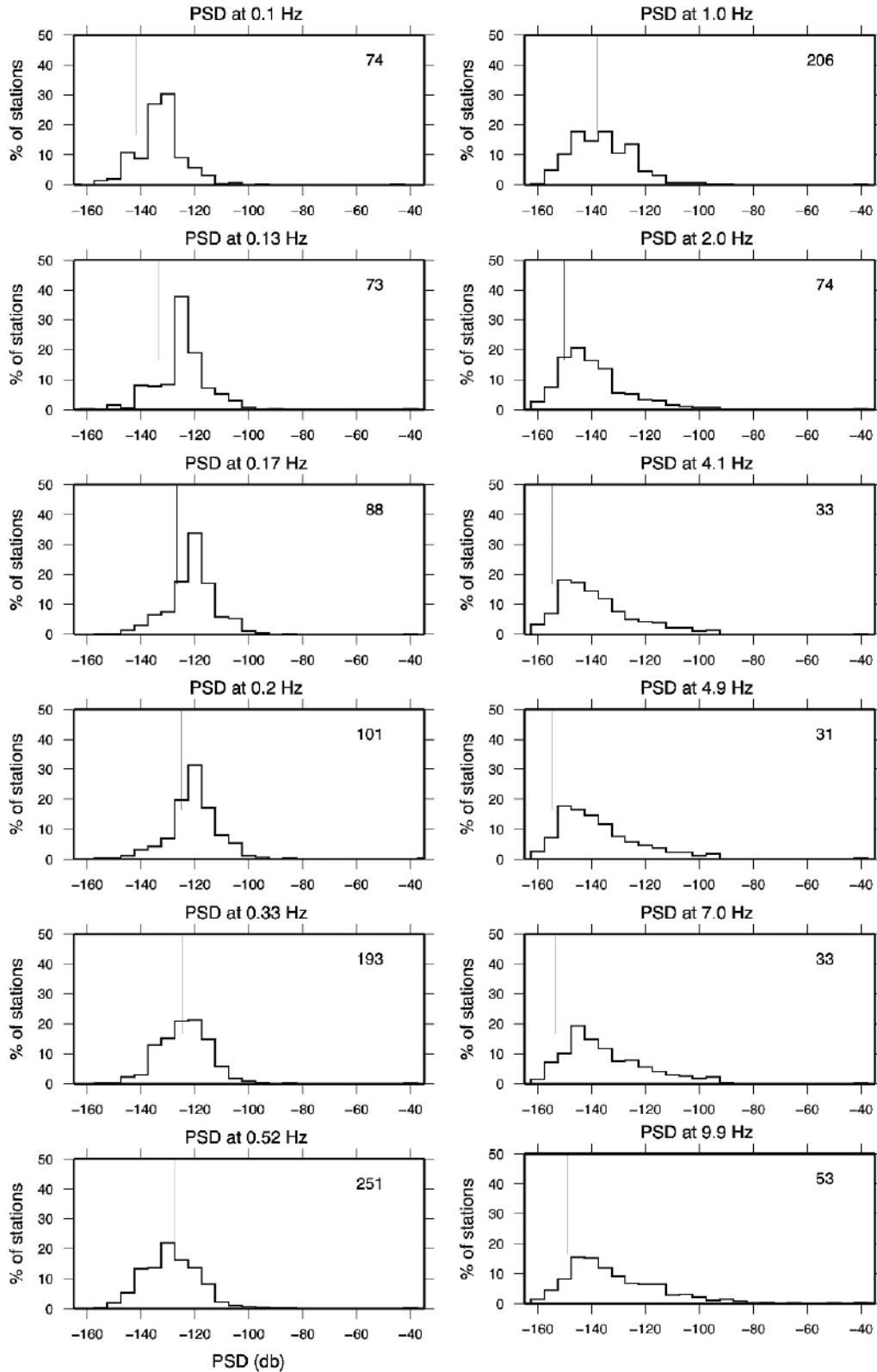
Fig.6. *ranking of the SOE2 station among the 445 stations of the Incorporated Research Institutions for Seismology virtual network FDSN+ALL in the period January-March 2020 [3]. For each frequency bin (indicated at the top of the panels) we calculate the mean PSD (in dB). The vertical bars indicate the average level of noise observed in SOE2 in the same time span, while the numbers indicate the ranking with respect to the selected global network.*

3.1 Amplitude-depth dependence.

A peculiar feature of Sardinia is the low seismic background even at surface, and it is related both to the geologic framework and to the low population density in the island. Nevertheless, we can observe a depth-dependent attenuation of the noise level in the underground stations of Sos Enattos compared to that of the surface station. In particular in **Fig.7** we show the 5th, 50th and 95th percentiles of the ratios of the amplitude spectral density for the vertical channels of SOE0 (surface) and SOE2 (-111m) [3]. At the underground level, the amplitude decay becomes relevant above 2 Hz, reaching a factor 5 at 10 Hz. In the figure the percentiles are compared to the theoretical ratios obtained from the synthetic Rayleigh-wave seismogram based on the velocity profiles measured in the Sos Enattos area [3]. The simulated Rayleigh-wave amplitude ratios are in good agreement with the measurements.
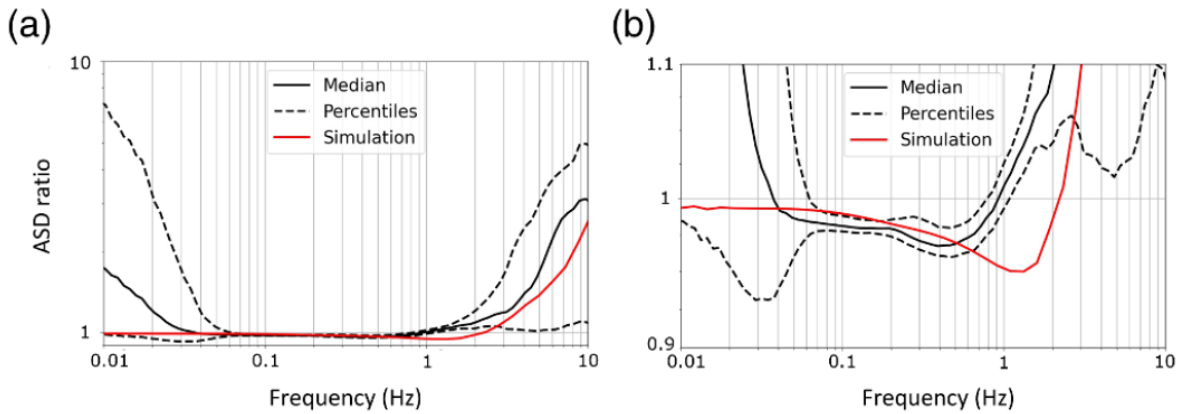

Fig.7. (a) Vertical component SOE0/SOE2 amplitude spectral density (ASD) ratio (median, black line) and 5th and 95th percentiles (dashed lines) compared with the corresponding amplitude ratios estimated from synthetic seismograms (red lined) [3]. (b) Zoom around ASD=1.

3.2 Horizontal-to-vertical spectral ratio

The horizontal-to-vertical ratios (HVSRs) of the measured seismic noise provide information about the elastic properties of the rocks in the area. Indeed, peaks in the HVSR correspond to the S-wave resonance frequencies [3], therefore the HVSR function helps constraining the elastic properties of the shallowest geological layers and can be used to evaluate the site amplification effects. We used four months of SOE0 data to calculate the HVSR shown in **Fig. 8**, where the average and the 5th and 95th percentiles are shown: the average value is about 1, and there are no peaks in the function, indicating that there are no significant amplification effects. We can also infer that there are not significant impedance contrasts down to depths of about 2500-3000 m [3].
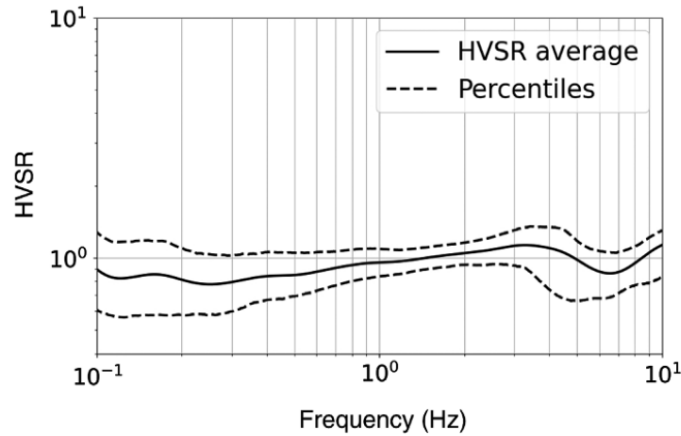
Fig.8. *Average horizontal-to-vertical ratio (HVSR) of SOE0 in the period 1 January - 30 April 2020 [3]. Dashed lines are the 5th and 95th percentiles.*

4. Seismic Velocities

Preliminary constraints on the ground velocity profiles at the site are obtained from the analysis of the ground motion associated with the drilling-and-blasting enlargement of a gallery of the mine. The blasting was conducted on 18 October 2018, and it consisted of five consecutive explosions fired at 0.25 s intervals, at a depth of about 150 m beneath the surface. We recorded the signals generated by the blasts using a linear array of five seismometers positioned at distances in between ~450 and 2000 m from the surface projection of the shot point. By fitting the first-arrival times with a straight line, we obtain an apparent P-wave velocity V_P of 4.80 +/- 0.13 km/s (**Fig. 9a**). We then use a frequency–time analysis of recorded data to estimate the Rayleigh-wave group velocity. First, we calculate the envelopes of the signals at individual stations, using a Gaussian filter with parameter α=10, spanning 25 center frequencies within the [3,8] Hz frequency interval. For each frequency, we use the time differences between the maxima of the envelopes at the different stations to derive group-velocity estimates for each independent station pair. For each frequency bin, we then average those velocity estimates, thus obtaining the dispersion relationship of **Figure 9c**. A p−ω stack procedure is then applied for deriving a phase-velocity dispersion curve over the [2.5,5] Hz frequency range (**Fig. 9c**). Under the assumption that both the group- and phase-velocity dispersions are associated with the fundamental mode of Rayleigh waves, we jointly invert those curves for a shear-wave velocity (V_S) profile. We conduct the inversion using the GEOPSY code, using a simple parameterization of the subspace consisting of two, 100-meter-thick layers overlying a half-space. Density is kept constant at 2600 kg/m^3 , whereas the Poisson ratio is let to vary in the 0.2–0.3 range. At the end of the inversion, we consider as acceptable those velocity profiles for which the corresponding dispersion curves are included in the 0.5 sigma interval around the experimental dispersions (**Fig. 9c**). Shear-wave velocities span the [1.8,2.0], [2.0,2.2], and [2.5,2.7] km/s intervals for the two layers and the half-space, respectively. The corresponding P-wave velocities, respectively, span the [3.1,3.6], [3.4,0.0], and [3.4,0.0] intervals. The retrieved model suggests a substantial homogeneity of the shallow velocity structure, in agreement with the lack of amplification effects discussed in the previous section.
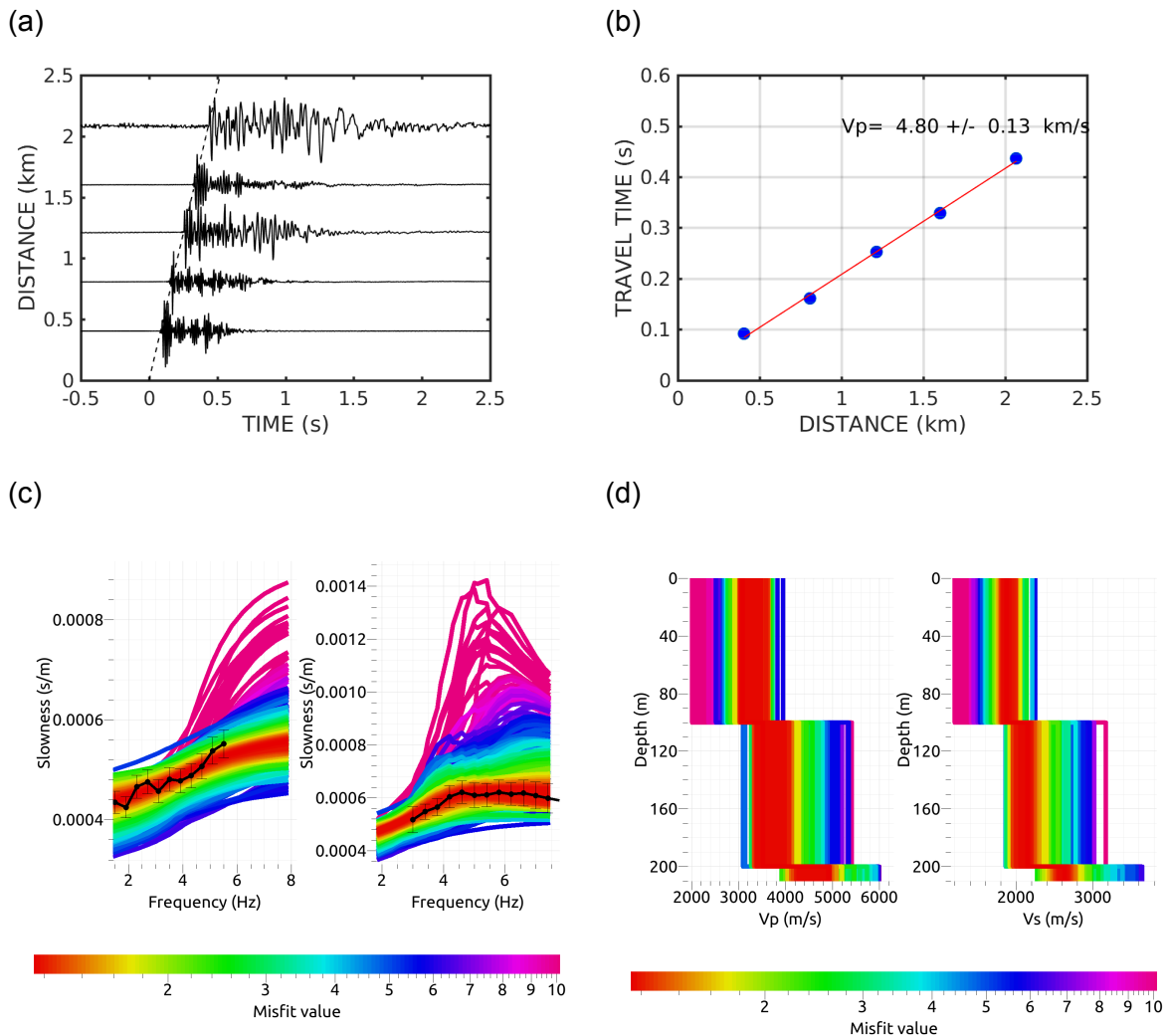
Figure 9. (a) Recordings of the vertical component of ground velocity associated with the blasting fired at 8:36:10 UTC on 18 October 2018. Traces are individually normalized to their maximum amplitude. (b) Apparent P-wave propagation velocity derived from the linear fit of P-wave arrival times as a function of the distance from the source. (c) Phase- (left panel) and group- (right panel) velocities measured over the [2,5.5] Hz and [3,8] Hz frequency intervals, respectively. The measured dispersion data are indicated by black dotted lines, and are compared to the predictions from the ensemble of investigated velocity models (colored patches). (d) Compressional- (left panel) and shear- (right panel) waves velocity models derived from the joint inversion of the phase- and group-velocity dispersions shown in (c). Colors in (c,d) correspond to the inversion misfit, according to the color bars at the bottom.

5. Earthquakes monitoring

The seismic waveforms from the stations operating at Sos Enattos can be used also to study the correlation between the seismometers. High correlation points indicate earthquakes, and this method can be used to search for local low-magnitude earthquakes that could be missed from the seismic monitoring of the area. Indeed, analyzing the data from 1 April 2019 to 31 August 2019 and from 1 January 2020 to 30 April 2020 we found a total of 69 seismic events (teleseism, i.e. far earthquakes) plus two extra peaks that are not reported e.g. in the INGV catalog. For these two low-magnitude events, P-S travel time difference suggests a local origin. In Fig.10 we show, as example, the correlations between SOE0-SOE2 and SOE1-SOE2 during a week of observation: in the first case it is evident the day-night pattern, while it is mild in the second case. The first two circled points in the figure show two earthquakes from Greece and Japan, while the third peak is a local event of magnitude M_L=1.8.
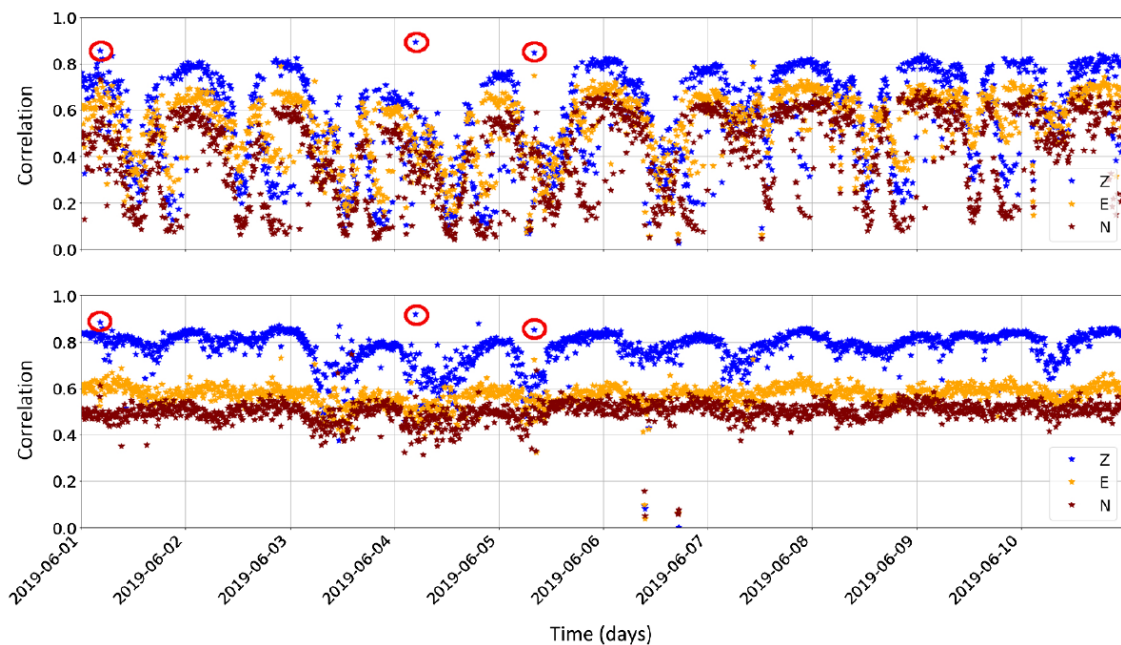

Fig.10. *Correlation between seismic stations versus time for nine days of June 2019 in the band 1Hz<f<10Hz for all the three channels (vertical and horizontals) [3]. In the top panel the correlation between SOE0 (surface) and SO2 (underground) is shown, the night-day pattern is evident. In the bottom panel the correlation between SOE1 and SOE2 (both underground) is shown, in this case with a mild night-day pattern only in the vertical channel. Red circles indicate three earthquake detections.*

6. Microseismic noise

In the microseismic band (0.1 - 1 Hz) the main source of seismic noise is the sea climate. In particular, it is possible to correlate the sea wave height, provided by the Copernicus Marine Environmental Monitoring Service (CMEMS), with the seismic PSD measured at Sos Enattos, as it is shown in **Fig.11** [3].
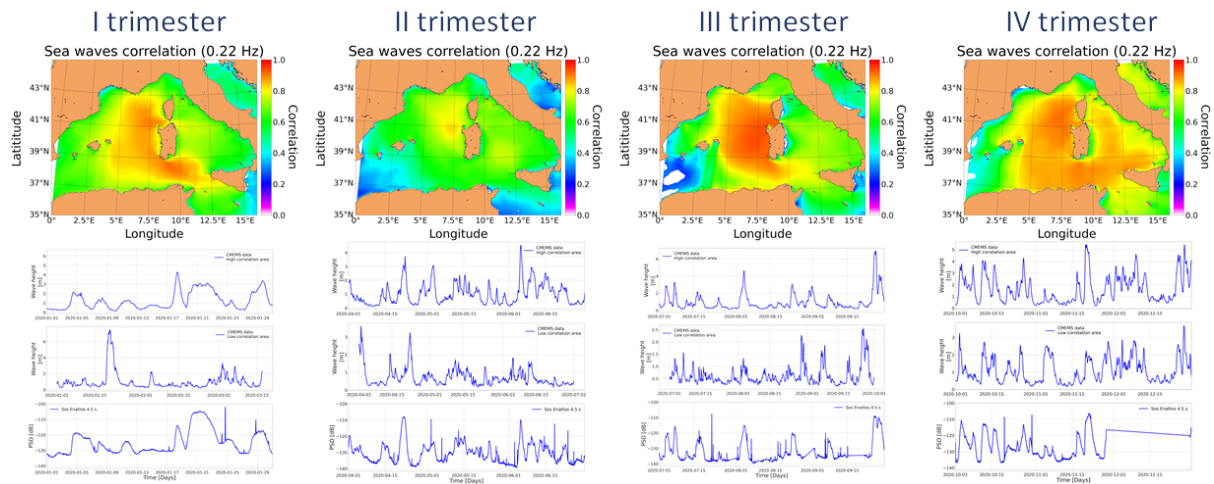
Fig.11. *Correlation between the average sea wave height from CMEMS and the seismic noise at Sos Enattos in 2020, each panel indicate a trimester, with the top sub panel showing the correlation in the Mediterranean sea around the island of Sardinia, and the low sub panel showing the wave height respectively for high and low correlation areas and the seismic PSD at 4.5s observed at Sos Enattos.*

We found the higher correlation for waves of period 4.5s, which corresponds to ground vibrations of frequency f = 0.22Hz, producing the main peak observed in the seismic PSDs. We were also able to localize the sea area where most of the observed microseism is produced, in the northwestern Mediterranean Sea (Gulf of Lion). Since it is related to sea climate, the microseismic trend follows a seasonal behaviour, as shown in **Figures 11** and **12**.
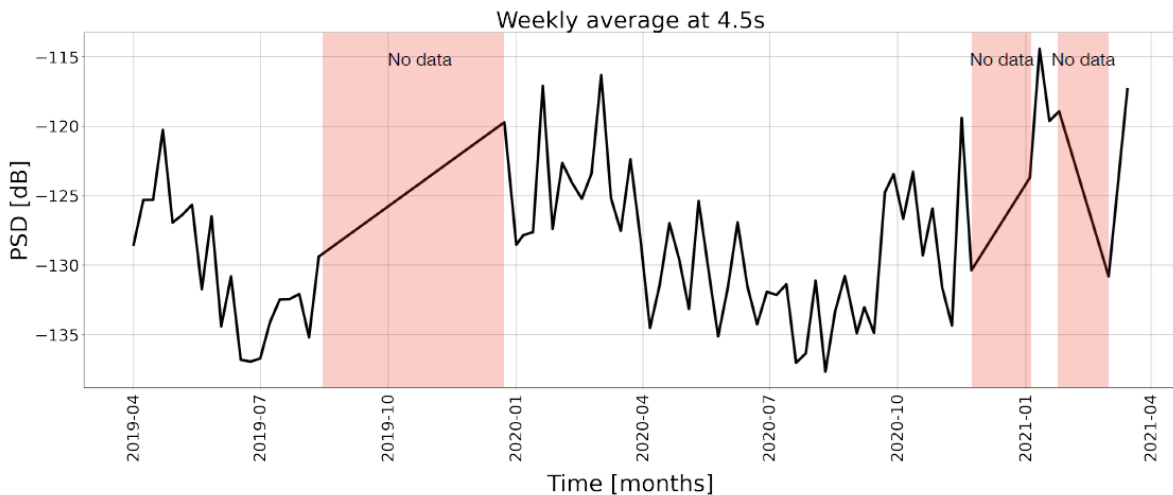

Fig.12. *Microseismic trend (PSD at 4.5s) observed at Sos Enattos in the period 2019-2021.*

7. Array measurements

For characterizing the space-time properties of the seismic noise wavefield at frequencies above 1Hz, we conducted a specific survey using a small-aperture seismic array composed by 15 stations deployed above the *Rampa Tupeddu*. Due to the rough morphology of the site, the array geometry was very asymmetrical, exhibiting a marked elongation along the NW-SE direction (**Fig. 13**)

For the experiment, we used 12 stations provided by the Mobile Seismic Network facility at INGV (COREMO), and three provided by UniSS. INGV stations consist of Reftek C130 24-bit data loggers, connected to Nanometrics Trillium SP120 sensors. UniSS's and UniNA's stations consist of Nanometrics Centaur 24-bit data loggers, equipped with Nanometrics Trillium 20s PH seismometers. All the array stations recorded in continuous mode at a sampling rate of 200 Hz from January 20 to February 5, 2021. On the early morning of January 22, 2021, stations A03 and A13 were burnt in a vandalism act, with an estimated economic loss on the order of 25KEur. For the rest of this report, therefore, data from those sites are not included.

Fig. 13. *Geometry of the surface seismic array deployed at Sos Enattos on January 2021.*

7.1 Spatial autocorrelation

Over the past 15 years, the correlation properties of the ambient noise have been widely exploited for retrieving either phase or group velocities of surface waves. Under the hypothesis of a horizontally-propagating stochastic wavefield, it is now well established that the azimuthal- or temporal-average of the narrow-band correlation coefficients between the signals recorded at two stations is directly related, through a 0-*th* order Bessel function, to the Rayleigh-wave phase velocity at that particular frequency. Thus, by measuring   the

zero-lag correlation coefficient for a certain station pair and subsequent, narrow frequency bands, one can obtain the phase velocity dispersion curve for the propagation path in between the two recorders.

Before calculating the correlation functions, noise recordings are subjected to a pre-processing procedure consisting of detrending, demeaning, tapering; in order to remove the effect of transient, large-amplitude signals of either natural or artificial origin, we adopted a running-absolute-mean normalization using a 5-s-long averaging window.

The spatial correlation coefficients are evaluated for all the independent station pairs in the frequency domain, over the [1,20]Hz frequency interval. Each correlation function is then fitted by a 0th order Bessel function, assuming that phase velocity c varies as a function of frequency f following a power law in the form: $c(f) = A\ exp(-b\ f)$, where the (A,b) coefficients are determined using a grid search procedure. Separately, we also evaluate the phase velocities using the first zero crossing of the correlation functions evaluated at different inter-station distances.

Figure 14 reports the velocity measurements obtained from the correlation analysis. Overall, the data are consistent with the previous estimates reported in Di Giovanni et al. (2020, [3]) from analysis of mine blast recordings (see **Fig. 9**). Within the 5-7 Hz frequency range, however, velocity data derived from the first zero-crossing of the correlation function are larger than those obtained from the mine-blast recordings. This discrepancy may be interpreted in terms of (a) contamination of higher propagation modes, (b) interference related to the sharp topography at the site, or a combination of both factors. Nonetheless, these results confirm that the site is characterized by high shear-wave velocities, even at very shallow depths.
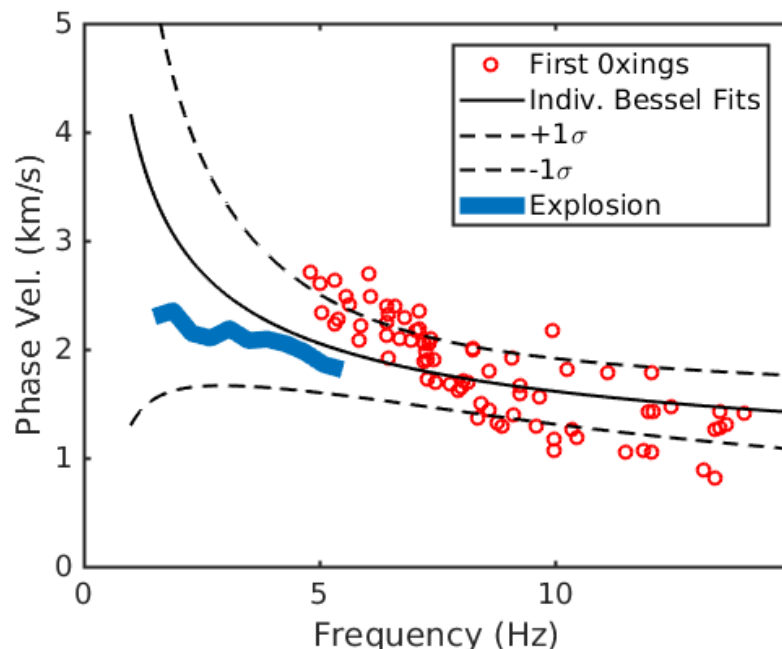

Fig. 14. Phase velocities derived from the first zero-crossing of the correlation functions (red circles), and through fitting individual correlation functions using power-law dispersions (black line). The blue stripe indicates the dispersion relationship obtained from analysis of mine blasting recordings (see Fig. 9).

7.2 Slowness analysis

Slowness analysis aims at determining the kinematic properties (i.e., apparent velocity and azimuth) with which coherent signals propagate across the array. Under the plane-wave assumption, slowness analysis is conducted using the classical minimum-variance distortionless (or High-Resolution) method of Capon (*High-resolution frequency-wavenumber spectrum analysis. Proceedings of the IEEE, 57(8), 1408-1418*, 1969). Narrow-band slowness power spectra are evaluated over a polar grid as a function of ray parameter r (i.e., the inverse of the modulus of the apparent velocity) and propagation azimuth φ. r is measured in s km^{-1}, and φ in degrees clockwise from the N direction. The procedure is iterated over time windows of length equal to 10 times the period corresponding to the reference frequency f_0, sliding along the array recordings by 50% of their length. A sample slowness power spectrum is illustrated in **Figure 15**; apparent velocity and propagation azimuth of the plane wave crossing the array are derived from the coordinates of the spectral peak.
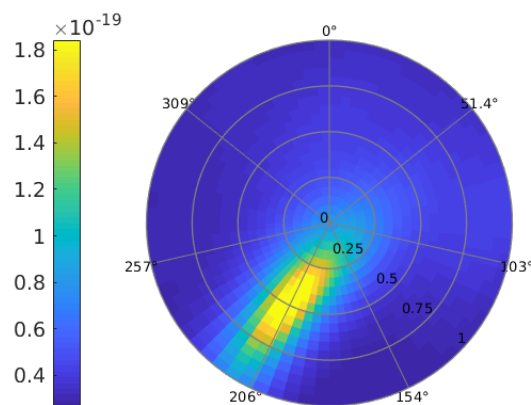

Fig. 15. Sample slowness power spectrum calculated over the 7-11Hz frequency band. The position of the spectral peak corresponds to a plane wave propagating with a ray parameter around 0.5 s km^{-1} (i.e., an apparent velocity of about 2 km s^{-1}), toward a direction ~210°N. The source is therefore located ~30°N of the array.

Figure 16 illustrates the temporal behaviour of spectral and propagation parameters for a sample 1-hour-long data interval. The spectral content of the noise signal is characterized by: (a) a time-stationary, main lobe at frequencies lower than 2 Hz, associated with the marine microseism; (b) transient events characterized by spectral lobes spanning the 8-20Hz frequency range, occasionally associated with peaks at frequencies of about 4.5 and 6 Hz.

Propagation parameters derived at frequency 6Hz indicate that the transient signals are mostly associated with propagation directions pointing to a bridge on Provincial Route SP73, visible at the right margin of the map reported in the bottom panel of **Figure 17**. In agreement with the correlation data discussed above, apparent velocities are generally larger than 2 km s^{-1}. These latter data must however be interpreted considering the large uncertainties due to both the reduced array aperture, and coarse sampling of the ray parameter space by the time of evaluating slowness spectra.
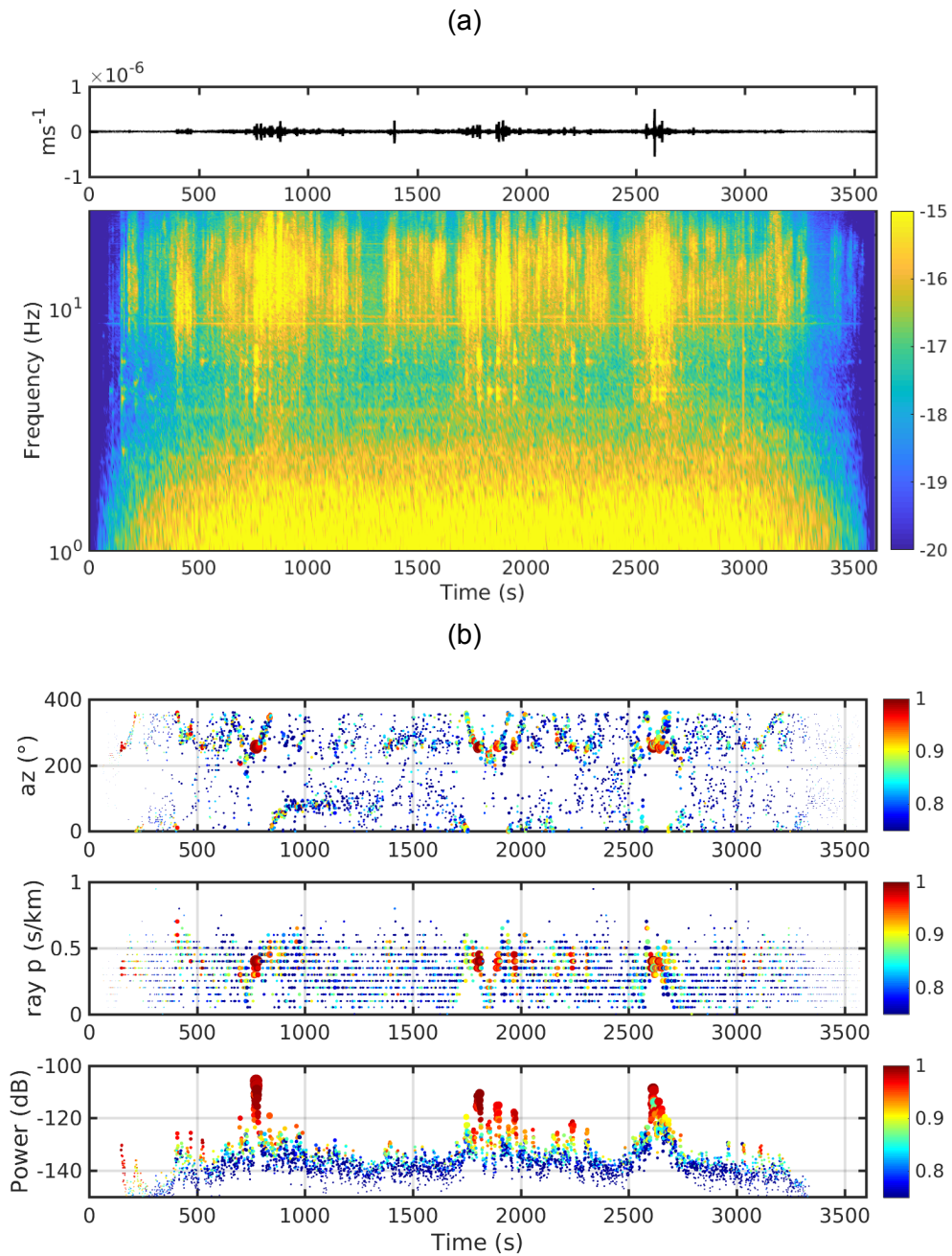
Fig. 16 - *(a) Sample vertical-component recording of ground velocity at array station A01 (top). Data are band-pass filtered over the 1-25 Hz frequency band to better highlight the contribution of cultural noise. At the bottom, the array-averaged distribution of spectral power as a function of time and frequency (spectrogram) of the same signal. Colors indicate the log10 of power, according to the color bar at the right. (b) Results from slowness analyses for the sample frequency of 6.0 Hz. From top to bottom, the panels report the propagation azimuth (measured clockwise from N), the ray parameter, and the power of the slowness spectrum. Symbols are sized according to the RMS amplitude of the signal, and colored according to the*

multichannel coherency (color bars at the right). The analyzed time interval has length 1 hour, and begins at 05:33:20 UTC on January 21, 2021.
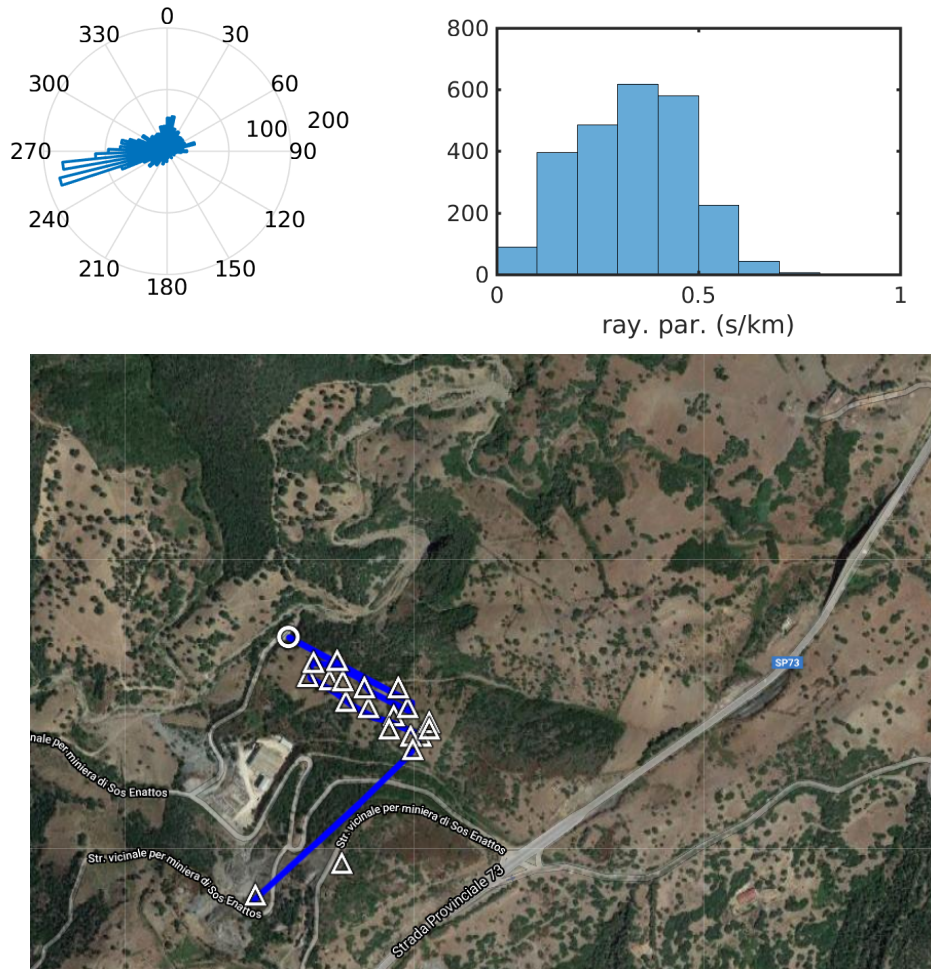

Fig. 17 - Top left: Rose diagram indicating the prominent directions of propagation derived from the slowness results shown in Figure 16. Only data associated with a coherency larger than 0.75 are considered. Top right: Distribution of ray parameters for the same time interval. Bottom: Enlarged map view of the array and surroundings. The observed directions of propagation suggest that most of the noise at frequency ~6Hz is associated with a bridge on Provincial Route SP73, visible at the right margin of the map.

7.3 Polarization analysis

The polarization properties of the noise wavefield are evaluated using the classical procedure based on the eigen-decomposition of the covariance matrix of the three components of ground motion. The principal axes of the covariance matrix define the polarization ellipsoid which best fits the particle motion trajectory. The polarization azimuth (measured clockwise from the N direction) and incidence (measured from the normal to the Earth's surface) angles are derived from the eigenvector associated with the largest eigenvalue. For the same data interval shown in **Figure 15**, the analysis is extended over a set of 20 log-spaced frequencies spanning the [1-10]Hz frequency interval. The corner

frequencies of the filter are set at 90% and 110% of individual reference frequencies. The procedure is iterated over subsequent time windows, whose length is equal to four times the period corresponding to the center frequency under analysis. **Figure 18** shows the distribution of polarization directions at station A10, evaluated over subsequent frequency bands. At frequencies below 2 Hz, the orientation is mainly directed toward NW. Di Giovanni et al. (2020, [3]) found that the main source of microseismic noise is located west of Sardinia and Corsica; such polarization directions are thus consistent with Rayleigh waves propagating from that source region. At frequencies above 2 Hz, the polarization directions are markedly frequency-dependent and, above 6 Hz, they are mainly oriented toward the North.
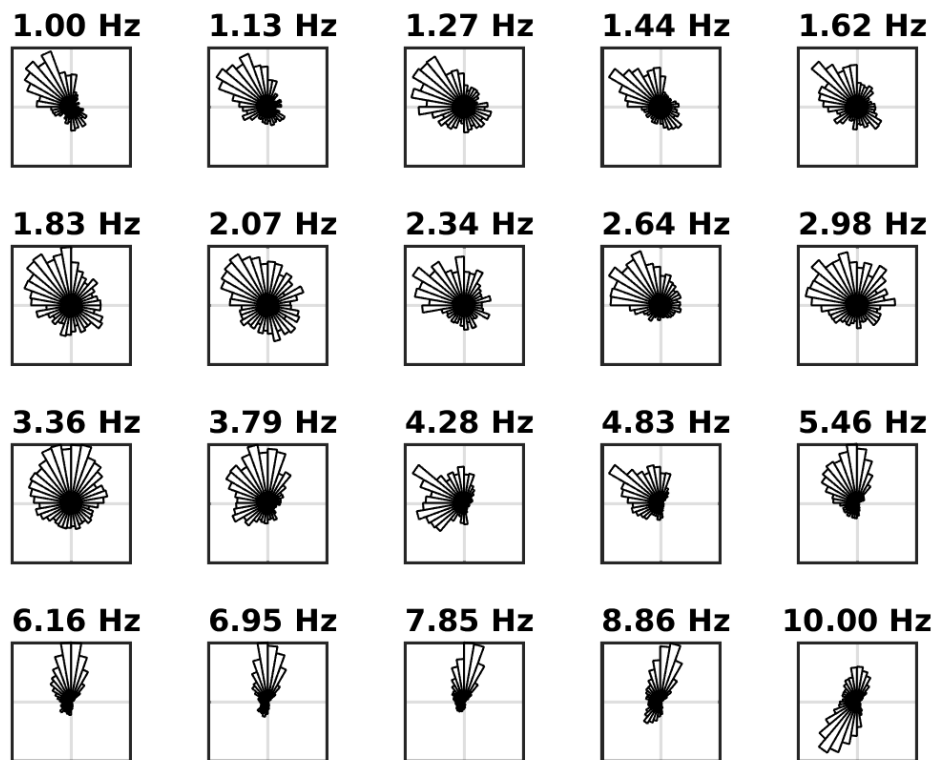

Fig. 18. Distribution of polarization azimuths at station A10 for a set of 20 center frequencies spanning the [1,10]Hz frequency band. The data interval is the same shown in Figure 16.

A further aspect to consider concerns the spatial variability of the polarization attributes. As a matter of fact, the dominant directions of particle motion at a single sample frequency do change from one site to another (**Figure 19**), making it difficult to associate a single wave-type to the noise wavefield.
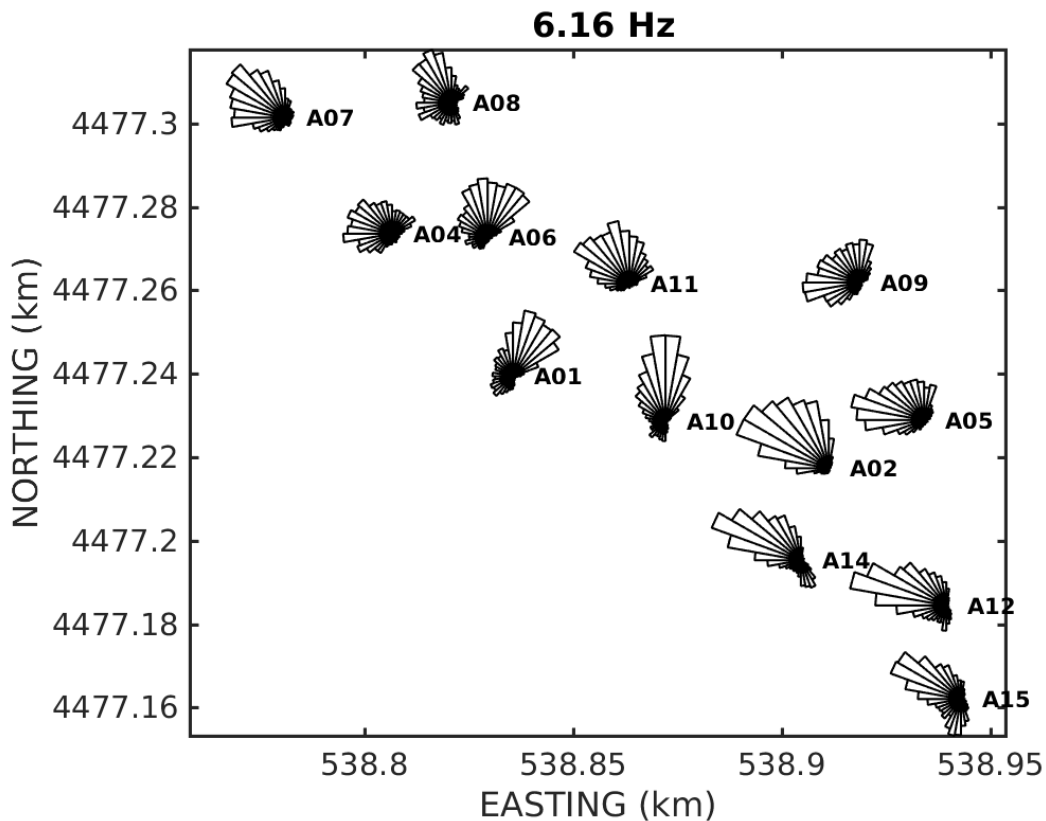
Fig. 19. *Distribution of the polarization azimuths at the different array elements, for a fixed reference frequency.*

In conclusion, the results obtained thus far from the array experiment at Sos Enattos indicate that:

I. Seismic noise of anthropogenic origin becomes dominant at frequencies above 2 Hz;
II. Within this band, the recordings are characterized by transient signals, whose energy is associated with spectral peaks of variable bandwidths (e.g., 4-5 Hz, 6Hz, 8-20 Hz); the energy associated with those peaks is coherently observed throughout the array deployment.
III. Polarization attributes indicate a marked spatial variability, as a likely consequence of topographic effects. At individual stations, the particle motion at frequency below 2 Hz exhibits a stable orientation toward WNW, consistent with Rayleigh waves propagating from the main source of microseismic noise located west of Sardinia and Corsica. At frequencies above 2 Hz, the polarization attributes are markedly frequency- and space-dependent; further investigations are needed to better understand this variability, and to infer the dominant wave types from the comparison with synchronous results from slowness analyses.
IV. The dominant direction of propagations at frequency ~6 Hz suggest that the noise source(s) are mostly associated with vehicle traffic along SP73, and in particular with 2 bridges located at distances of ~500m and ~1000m from the array.

All these considerations need to be further corroborated by extending the analysis to the two horizontal components of ground motion, and considering longer time windows and different frequency bands.

8. Newtonian Noise projection of seismic glitches

At low frequencies, seismic glitches may limit the sensitivity of the Einstein Telescope. In particular, a typical Intermediate Mass Black Holes (IMBHs) could stay in the ET detection band below 10Hz for a time duration of the order of one minute. We can use this time window to analyze the observed seismic noise searching for seismic glitches that would potentially spoil the IMBH detection in this band.

Defining the Newtonian noise contribution to the detector output dependent on the observed seismic displacement, as explained in [4], it is possible to plot the preliminary Newtonian noise projection for ET shown in **Fig .20**, calculated taking the seismic data measured underground at Sos Enattos in SOE1. As can be seen, the Newtonian noise projection is below the ET target sensitivity in the low-frequency down to 2.6Hz, reaching a factor 2 higher than requirement only at 2Hz. This implies that, based on these preliminary seismic measurements, a factor 2 Newtonian Noise subtraction would be required only below 3Hz. It is important to note that this is only a preliminary projection, since ET will be probably deeper than SOE1, and a better seismic noise measure could be provided by borehole seismometers that will be installed at -250m in the Bitti and Onanì corner sites.
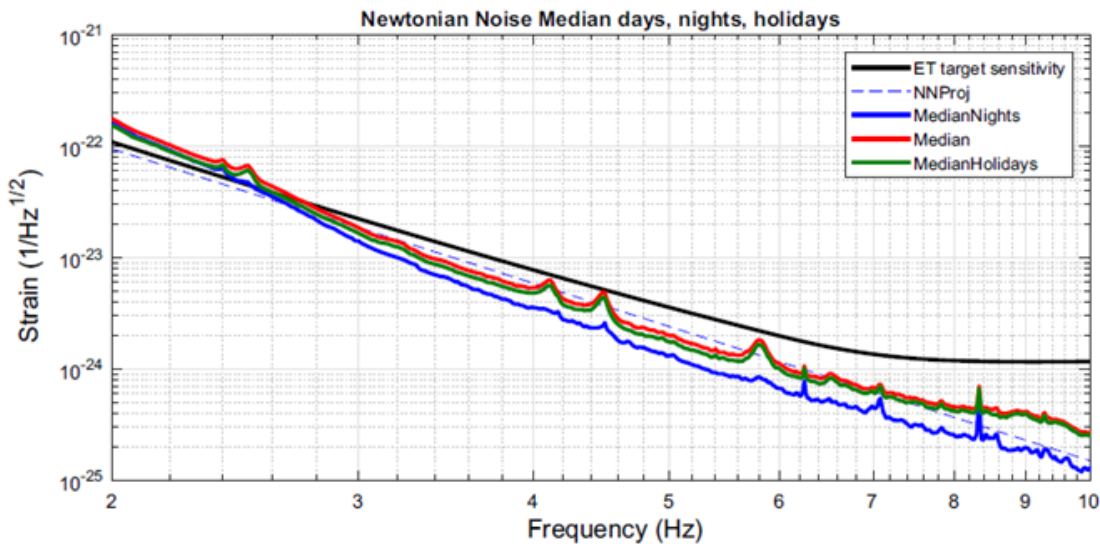

Fig.20. Amplitude Spectral Density of the ET target sensitivity (black) compared to the target Newtonian noise contribution (dashed line) and to the Newtonian noise projection calculated from the seismic noise measured in SOE1 (median in red, median for the nights in blue, median for weekends in green) [4].

It is also possible to study the distribution of the observed transients in the seismic noise at Sos Enattos, defining a noise-to-target ratio (NTR) of the Newtonian noise with respect to the ET sensitivity as defined in [4]. Doing so, a value of NTR<1 indicates that the Newtonian noise is below the ET target sensitivity. The results of this analysis, considering the seismic data acquired in SOE1, is reported in **Fig.21** [4]. The probability of having the Newtoian noise below the detector target sensitivity is: $P(NRT<1)=0.6$, and it increases if we consider only the data measured in the nighttime: $P(NRT<1)_n=0.86$.

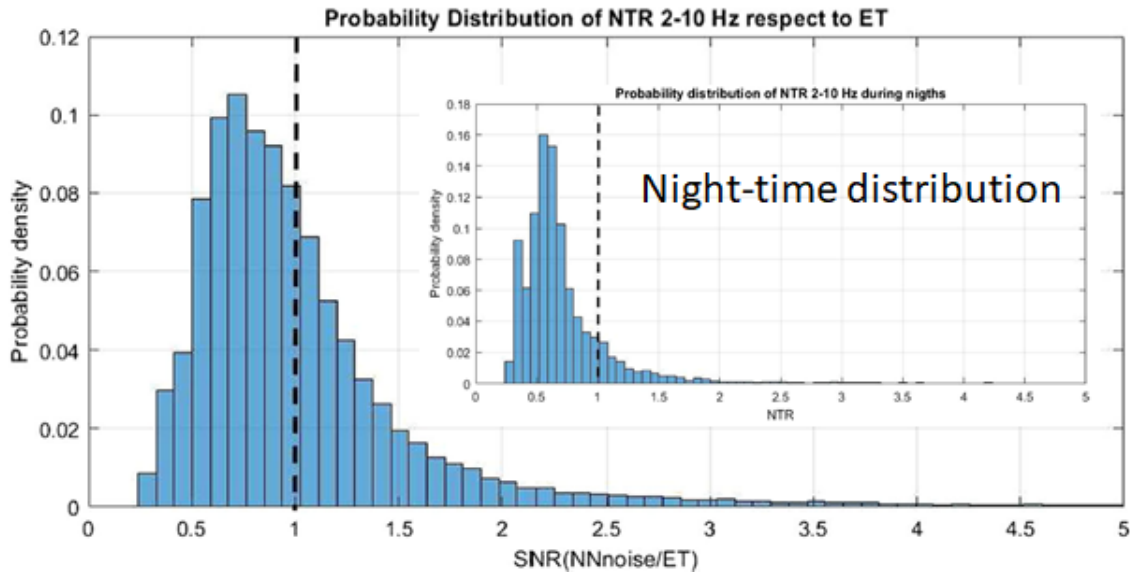***Fig.21.*** *Noise-to-target ratio (NRT) probability distribution over the whole period [4].*

9. Bibliography

[1] L. Naticchioni *et al.,* **Microseismic studies of an underground site for a new interferometric gravitational wave detector**, *Class. Quantum Grav.* **31** 105016, 2014

[2] L. Naticchioni *et al.*, ***Characterization of the Sos Enattos site for the Einstein Telescope***, **JPCS** 1468, 2020

[3] M. Di Giovanni *et al.*, ***A seismological study of the Sos Enattos Area – the Sardinia Candidate Site for the Einstein Telescope***, **SRL**, 2020 https://doi.org/10.1785/0220200186

[4] A. Allocca *et al.*, ***Seismic glitchness at Sos Enattos site: impact on intermediate black hole binaries detection efficiency***, **EPJP**, 2021 https://doi.org/10.1140/epjp/s13360-021-01450-8